

# High-energy femtosecond laser pulse compression in single- and multi-ionization regime of rare gases: experiment versus theory

T. Auguste · C. Fourcade Dutin · A. Dubrouil ·  
O. Gobert · O. Hort · E. Mével · S. Petit ·  
E. Constant · D. Descamps

Received: 3 October 2012 / Accepted: 11 December 2012 / Published online: 8 January 2013  
© Springer-Verlag Berlin Heidelberg 2013

**Abstract** We report experimental and numerical results on the post-compression of 40 fs duration pulses down to 10 fs at high energy level (multi-mJ). The spectral broadening is achieved through the self-phase modulation resulting from optical-field-ionization of different noble gases (He, Ne, Ar) by the 40-fs laser pulse propagating in a low-pressure gas-filled hollow capillary. We discuss the influence of the multi-ionization dynamics, through the gas dependence, on the laser energy carried by the capillary, as well as on the duration and temporal shape of the post-compressed pulses. In all the different experimental conditions investigated in this article (pressures and gases used), the experimental data is in good agreement with the numerical results from a three-dimension propagation code. Through this study, we demonstrate the robustness of the proposed post-compression technique with regard to multi-ionization, indicating that it can be used on a large intensity range by judiciously choosing the gas.

## 1 Introduction

Nowadays, further progress in strong-field physics often requires multi-terawatt laser systems with pulse durations of 1–2 optical cycles. Among other applications of current

interest, attosecond physics ( $1 \text{ as} = 10^{-18} \text{ s}$ ) using high-order harmonic generation (HHG) in gases or on solid targets are domains requiring such lasers [1, 2]. Indeed, both high power and short pulses are necessary for generating bright extreme ultraviolet (EUV) single attosecond bursts [3–9] in order to probe intra-atomic and intramolecular electron dynamics [10–13]. Several sub-terawatt laser systems with few optical cycle pulse duration already exist and are now routinely used worldwide. These systems are mainly based on the recompression of longer pulses of few tens of femtosecond duration. They use the spectral broadening due to Kerr induced self-phase modulation (SPM) in a gas, either in a self-guided filament [14] or in a high-pressure gas-filled hollow capillary [15–18] in order to obtain the bandwidth required to achieve such short pulses. In both configurations, the input power is limited by the critical power for self-focusing [19], above which the laser beam breaks up into several filaments [20]. So far, the best performance using Kerr-induced SPM in a gas is 1 terawatt peak power (5 mJ–5 fs) and is obtained by focusing chirped input femtosecond pulses in a helium-filled hollow capillary with a pressure gradient [17]. Another approach to produce few optical cycle pulse duration at high peak power level is to use optical parametric chirped-pulse amplifiers (OPCPA) in non-collinear geometry [21, 22]. Through a mixed laser architecture based on high-pressure neon-filled hollow capillary as a front end for non-collinear OPCPA, Herrmann et al. [23] have demonstrated the generation of 7.9 fs–130 mJ laser pulses. However, this is a very sophisticated and expensive approach, which requires completely new designs and high-energy picosecond pump laser. As an alternative to these costly systems, we recently proposed and experimentally demonstrated the post-compression of a standard 70 mJ, 40 fs Ti: Sapphire laser system down to 11.4 fs,

---

T. Auguste (✉) · O. Gobert  
CEA-Saclay, IRAMIS/Service des Photons,  
Atomes et Molécules, 91191 Gif-sur-Yvette Cedex, France  
e-mail: thierry.auguste@cea.fr

C. Fourcade Dutin · A. Dubrouil · O. Hort ·  
E. Mével · S. Petit · E. Constant · D. Descamps  
Université de Bordeaux—CNRS—CEA,  
Centre Lasers Intenses et Applications, UMR5107, 351,  
cours de la Libération, 33405 Talence Cedex, France

with a total output energy per pulse of 13.7 mJ, using an efficient and robust spectral broadening technique [24]. To obtain the required spectral bandwidth, we used the SPM resulting from the optical-field-ionization (OFI) of helium gas by the 40-fs laser pulse while propagating in a low-pressure gas-filled hollow capillary. We further carried out a detailed numerical study, which reproduces very well the experimental measurements. Three-dimension (3D) simulations unambiguously show that it is necessary to carefully filter the fundamental mode of the capillary, in order to obtain a spatially homogeneous smooth post-compressed pulse [25].

The key idea of the method is that the refraction index of a medium subject to OFI varies rapidly during the ionizing pulse, generating new frequencies mainly in the blue wing of the spectrum. In a one-dimensional (1D) approach and in the case of a low-density plasma ( $N_e(t) \ll N_c$ ), the pulse instantaneous frequency after propagation through a homogeneously ionized gas of length  $L$  is given by [26]:

$$\omega(t) = \frac{d\varphi}{dt} = \omega_0 + \frac{\omega_0 L}{2cN_c} \frac{dN_e(t)}{dt}. \quad (1)$$

where  $t$  denotes the time,  $\omega_0$  the input pulse carrier-frequency,  $N_e$  the free-electron density, and  $N_c = \frac{m\epsilon_0\omega_0^2}{e^2}$  the critical density ( $N_c = 1.7 \times 10^{21} \text{ cm}^{-3}$  at 808 nm).

Since OFI is very fast and highly nonlinear, large spectral broadenings can be achieved, even with low gas pressures and moderate interaction lengths. For example, if one considers a singly ionized gas, a 1 mbar pressure, an interaction length of 20 cm and an OFI-time of 20 fs, one obtains a relative spectral broadening  $\Delta\omega/\omega_0 \sim 0.2$ . Experimentally, broad spectra have been obtained [24] with a few millibars of helium gas pressure, 40-fs laser pulse durations and several tens of millijoules of laser energy ( $P \sim 2 \text{ TW}$ ). Since critical power for self-focusing reaches 300 TW at 1 mbar helium pressure, higher pulse energy could be post-compressed, in principle, by using ions with higher ionization potential ( $I_p$ ). The study of such multi-ionized targets in OFI post-compression technique is the aim of this article. To test this possibility, we consider the case where post-compression can be achieved either with single ionization (helium) or with multi-ionization (neon and argon).

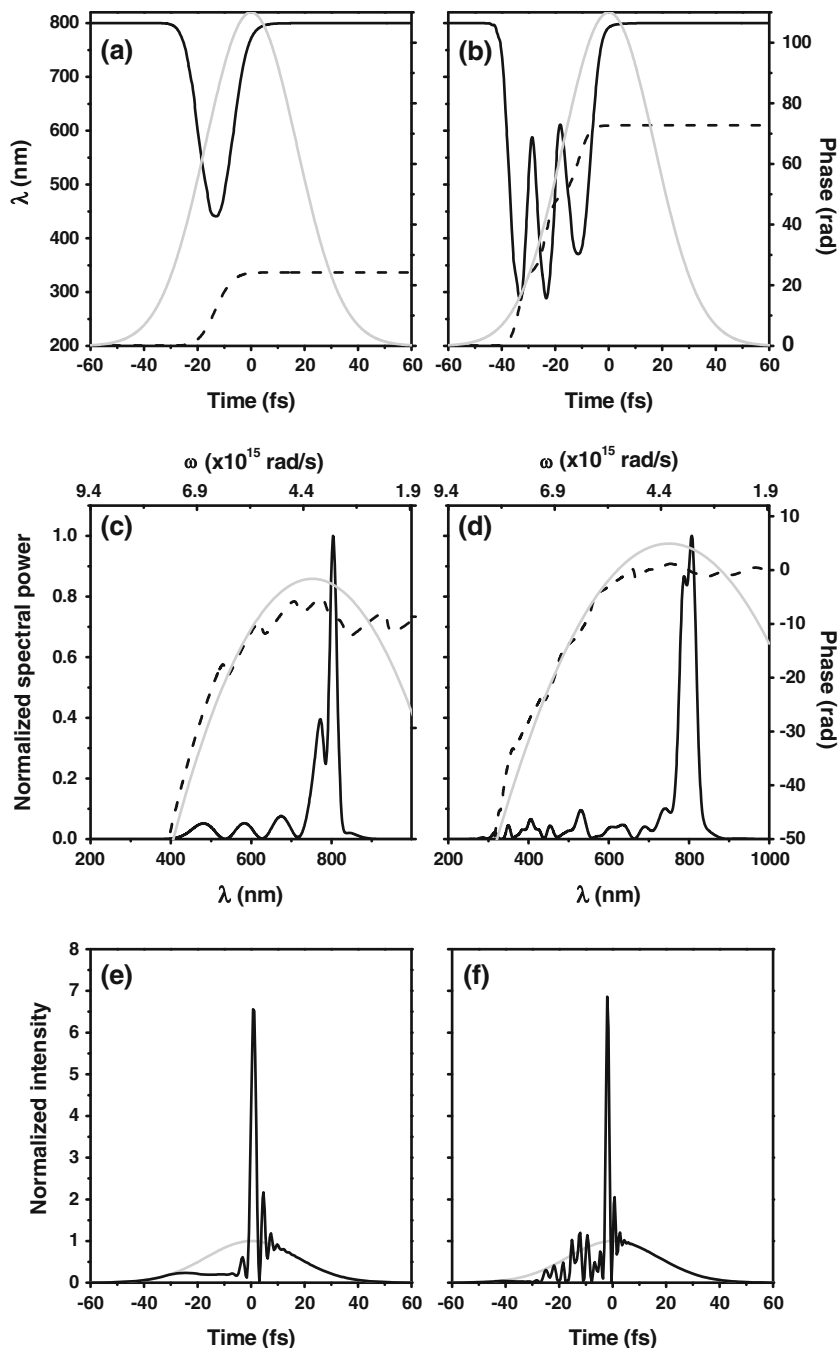
In this article, we present both experimental and numerical results on post-compression obtained with different noble gases: helium, neon and argon. By comparison with our previous works [24, 25], we use neon and argon gases instead of helium gas in order to get a higher ionization charge state with the same input laser intensity, and then to increase the spectral broadening, or alternatively, to achieve the same broadening (as with helium gas) with a lower intensity. In the latter case, the aim is to study the

possibility of extrapolating the post-compression technique, demonstrated in [24], to moderate-energy ( $\sim 10 \text{ mJ}$ ) high-repetition rate ( $\sim 1 \text{ kHz}$ ) laser systems. By using Ne or Ar as filling gas, important questions thus arise about the changes of spectral features (amplitude and phase) induced by the complicated ionization dynamics involved in the production of multiply charged ions, and also about ionization-induced refraction, which could cause some changes in the energy transmitted in the fundamental mode of the capillary, but also in the spatial, spectral and temporal properties of the recompressed output pulse. Using a simple one-dimension (1D) model, we discuss qualitatively, in Sect. 2, the influence of the ionization dynamics on the spectrum shape (bandwidth and amplitude modulations) for the different gases, and on the resulting recompressed pulses. The influence of the gas used on the laser energy transmitted by the capillary, as well as on the duration and temporal shape of the post-compressed pulse is then quantified using a recently developed 3D numerical model, which solves the equation of propagation of the laser field in the paraxial ( $\frac{\partial^2}{\partial z^2} \ll k_0 \frac{\partial}{\partial z}$ ) and slowly ( $\frac{\partial^2}{\partial t^2} \ll \omega_0 \frac{\partial}{\partial t}$ ) varying envelope approximations, assuming cylindrical symmetry, coupled to the ionization rate equations [25]. After a brief description of the experimental setup in Sect. 3 and of the 3D code in Sect. 4, we compare, in Sect. 5, the experimental data with the numerical results. We show how the ionization dynamics impacts on the spectral amplitude and phase of the pulse at the output of the hollow gas-filled capillary, and on the subsequent post-compressed pulse profile. The conclusion is given in Sect. 6.

## 2 Multiple ionization dynamics

In order to get an insight into the influence of the multiple ionization dynamics on the spectral broadening, we developed a simple 1D model based on the temporal phase modification of the ionizing pulse (Eq. 1) in a case of a 40 cm long homogeneous medium, a 1 mbar gas pressure and a 40-fs (FWHM) duration Gaussian pulse. The electron density is obtained by solving the coupled rate equations on the ion populations. The laser electric field-dependent ionization rates are calculated with Perelomov, Popov and Terent'ev (PPT) formula [27–29], adapted to complex atoms following Ammosov, Delone and Kraïnov (ADK) modifications [30]. We have reported in Fig. 1, the results for the two extreme cases, i.e., He (left column) and Ar (right column) gases at  $2.0 \times 10^{15} \text{ W/cm}^2$  intensity. Figure 1a, b give the instantaneous wavelength (solid line) and the temporal phase (dashed line). For a laser intensity of  $2.0 \times 10^{15} \text{ W/cm}^2$ , ionization of both gases occurs on the leading front of the pulse. In helium case, the ionization

**Fig. 1** **a, b** Instantaneous wavelength (*solid lines*) and temporal phase (*dashed lines*) calculated for **a** He and **b** Ar gases, and for  $2.0 \times 10^{15}$  W/cm<sup>2</sup> laser intensity. The *light grey line* gives the intensity temporal shape. The initial pulse duration is 40 fs, the medium length is 40 cm and the gas pressure is 1 mbar. **c, d** Normalized spectral profiles (*solid lines*) and spectral phases (*dashed lines*). *Light grey lines* are second degree polynomial fits of spectral phases. **e, f** Temporal profile of the ‘post-compressed’ pulses. Intensities are normalized to the initial peak intensities



state peaks to  $Z_{\text{ion}} = 1$  ( $Z_{\text{ion}} = N_e/N_a$ , with  $N_e$  the electron density and  $N_a$  the initial density of atoms), near the maximum of the pulse envelope (depicted by a light grey line in Fig. 1a). The corresponding instantaneous wavelength ( $\propto \frac{dN_e}{dt}$ ) reaches 450 nm, and the same wavelength is produced at most twice in the pulse, thus limiting interferences in the spectral domain responsible for strong amplitude modulations. The temporal phase ( $\propto N_e$ ) increases monotonously up to the peak intensity and is constant beyond. In contrast, with Ar gas, multi-ionization leads to modulations of the phase, corresponding to the production

of successive ionization charge states up to  $Z_{\text{ion}} = 3$ , and to an instantaneous wavelength up to 300 nm (Fig. 1b). In the case of argon gas, the same wavelength is generated several times during the rising front of the pulse. Surprisingly, the spectra (Fig. 1c, d) obtained by Fourier transforming the pulse envelope of the electric field corrected from the ad-hoc temporal phase, exhibits in both cases (helium or argon gas) a large quadratic phase component, as shown by the second degree polynomial fits of spectral phases in Fig. 1c, d (light grey lines), while spectral amplitudes are quite similar with a prominent feature around the initial

wavelength. The time profiles of the ‘post-compressed’ pulses, deduced from data of Fig. 1c, d, obtained by cancelling the quadratic spectral phase component, are also very similar, as shown in Fig. 1e, f. The maximum intensity of the ‘post-compressed’ pulses is enhanced by a factor of  $\sim 6$ – $7$ , near time  $t = 0$ , where the intensity of the initial 40 fs pulse is maximum (light grey line), with pulse duration around one optical cycle (1 cycle = 2.7 fs at 808 nm wavelength). In this 1D approach, the trailing edge of the initial pulse is not affected by OFI since electron density remains almost constant after the peak intensity. On the leading front of the pulse, the contrast is rather constant in the case of He gas, by comparison with Ar in which a multi-peak structure appears. This difference comes from the multi-ionization dynamics.

The above results thus suggest that even though the ionization dynamics is complicated by the production of multiply charged ions (spectral amplitude modulations and phase jump associated with a change of the ionization charge state), the use of elements heavier than He, with low ionization potential, allows us to achieve large spectral bandwidths, while keeping a nearly quadratic spectral phase. However, it must be stressed that this simple 1D model is not sufficient as it does not take into account propagation effects. In particular, it does not describe ionization-induced refraction, which is responsible for optical losses through capillary walls. For given intensity and pressure, it is much stronger in multi-ionized gases [31], because of sharp radial electron density gradients close to the central part of the laser beam. Moreover, in the special case of a hollow-core capillary, multiple ionization couples the laser energy in high (spatial) eigenmodes of the capillary, propagating with different group velocities and with different damping lengths, as will be discussed in Sect. 5.

### 3 Experimental setup

The experiments are performed with a 2 TW chirped-pulse-amplification (CPA) based on Ti:Sapphire laser delivering 70 mJ, 40 fs pulses at 10-Hz repetition rate. The beam has a 20 mm diameter and a quasi-flat-radial intensity profile. The CPA compressor and the post-compression setup (Fig. 2) are maintained under vacuum with typical pressure around  $10^{-6}$  mbar. The linearly polarized beam is focused by a spherical mirror M1 ( $f = 3$  m) to a waist  $w_0 = 140$   $\mu\text{m}$  (measured at  $1/e^2$  of the intensity maximum) and coupled into a capillary with a 420  $\mu\text{m}$  inner diameter (chosen to match the input beam to the  $\text{EH}_{11}$  mode [32]). We use a 40-cm-long capillary (4.5 times the Rayleigh range of the input beam), thus providing sufficient guiding to ensure a spectral broadening that is homogeneous across the transverse beam section while keeping the setup rather

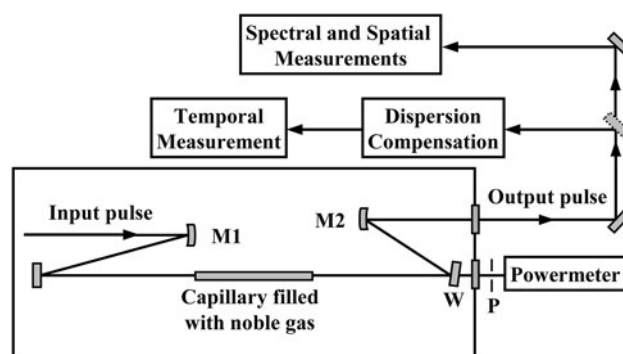


**Fig. 2** Post-compression setup. M1, focusing dielectric mirror with  $f = 3$  m; W, wedged window; M2, spherical silver mirror  $f = 2$  m; P, iris. The hollow capillary radius is 210  $\mu\text{m}$  and the length is 40 cm

compact. The gas injection in the capillary is achieved through a hole drilled in the capillary wall. In these conditions, the maximum energy transmitted through the capillary without gas, in the  $\text{EH}_{11}$  mode, is 27.3 mJ, corresponding to a  $\sim 40$  % capillary transmission whatever the input pulse intensity over the explored range. The capillary transmission results from the roughness of the capillary inner wall, the gas injection hole and the spatial quality of the input beam. Concerning this last point, we have measured the beam wavefront (HASO system from Imagine Optic) at the output of the compressor, and estimated a Strehl ratio of 0.6, leading to a maximum intensity of  $3.2 \times 10^{15}$   $\text{W}/\text{cm}^2$  at the entrance of the capillary. Two meters behind the capillary, a wedged window splits the beam in two parts. The transmitted beam, which carries out 92.2 % of the output energy, is used to measure the energy in the  $\text{EH}_{11}$  mode. The latter is spatially selected by means of a 15-mm-diameter iris P. The 4 %-energy beam reflected by the front side of the wedge ( $1^\circ$  apex angle) is collimated by a spherical silver mirror M2 ( $f = 2$  m) and exits the vacuum chamber through a 3-mm-thick BK7 AR-coated window. This beam is then used for spectral, spatial and temporal characterizations. It must be stressed that its intensity is weak enough to avoid additional non-linear effects. The far-field beam spatial profile is imaged onto a charged-coupled-device (CCD) camera in order to optimize the coupling into the capillary. Without gas, a well-defined circular and collimated beam with a diameter of 5.6 mm (measured at  $1/e^2$  of the intensity maximum) is observed. When the capillary is filled with a gas (He, Ne or Ar), the beam size is slightly smaller, and a weak light background appears over the whole CCD area. These observations indicate that plasma refraction induces some coupling to higher-order modes of the capillary. As expected, they also confirm the absence of filament whatever the gas used since critical powers for self-focusing are much higher than the one used in this experiment (for 1 mbar pressure, the critical power is 120 TW with Ne gas

and 10 TW with Ar gas). Finally, the output pulse compression is achieved through six pairs of negatively chirped-mirrors, with group velocity dispersion (GVD) of  $-40 \text{ fs}^2$  per bounce in the 650–1,000 nm wavelength range in order to overcompensate the output pulse chirp, and with silica plates of variable thickness to finely adjust the dispersion compensation. The overall transmission of the dispersion line is 80 %. The pulse duration is measured with a single-shot autocorrelator designed for sub-10 fs measurements and the residual spectral phase of the shortest post-compressed pulses is further characterized with a single-shot second-harmonic-generation frequency resolved optical gating (SHG-FROG) [33].

#### 4 Description of the 3D numerical model

The 3D numerical model used in the present article has been described in a previous article [25]. Briefly, the non-linear envelope equation governing the evolution of the laser field propagating in the forward direction is solved in the frame moving at the group velocity of the pulse [34]. The model takes into account the diffraction of the beam, the GVD, the Kerr effect (leading to self-focusing in the spatial domain and to SPM in the spectral domain), the spatio-temporal evolution of the plasma (leading to beam refraction and SPM) and their associated self-steepening, and the laser energy absorption due to the gas ionization. In the particular case of low pressure gas considered in the present work, we can actually neglect both GVD of the gas and Kerr induced SPM since they are pressure dependent. This has been confirmed by simulations performed by alternatively neglecting one or the other effect. The equation of the laser field propagation is solved self-consistently with the coupled rate equations giving the local electron density. The ionization rates are calculated using PPT formula. The number of charge states, taken into account in the electron density calculation, depends on the gas used:  $Z_{\max} = 2$  for He and Ne, and  $Z_{\max} = 4$  for Ar atoms.

To take full advantage of the properties of electromagnetic waves propagating in dielectric cylindrical waveguides, we write the linearly polarized electric field inside the capillary as the superposition of eigenmodes [19, 35]:  $\hat{E}(r, \xi, \omega) = E_{\max} \sum_{\ell, j} b_{j\ell}(\xi, \omega) J_{\ell} \left( \frac{\rho_j r}{a_0} \right)$ , where  $E_{\max}$  is the maximum field amplitude,  $J_1 = 0, 1, \dots$  is the Bessel function of order  $l$ ,  $\rho_j$  is the  $j$ th root of  $J_1$ , and  $a_0$  is the radius of the capillary. We assume that the laser pulse is initially coupled in the fundamental mode, proportional to  $J_0$ . The integration of the non-linear part of the propagation equation is performed using a fifth-order Runge–Kutta formula with Cash–Karp coefficients [36].

In the simulation results reported below, the laser electric field is expanded on 20 eigenmodes ( $\text{EH}_{1j}$ ,  $j = 1-20$ ), but we observed that the energy is mainly distributed between the fundamental and the four lowest excited modes. The laser electric field  $E(r, \xi, \tau)$  is computed on a  $(r, \xi)$  grid, with step sizes  $\Delta r = 0.5 \mu\text{m}$  in the transverse direction, and  $\Delta \xi = 100 \mu\text{m}$  along the propagation direction, respectively. The time integration is performed using a  $\Delta \tau = 0.15 \text{ fs}$  step size.

We consider a 40-cm-long capillary with  $420 \mu\text{m}$  inner diameter ( $2a_0$ ), uniformly filled with gas. At the input of the capillary, we assume a laser pulse with a Gaussian temporal shape of 40 fs full-width at half-maximum (FWHM) duration and a  $J_0^2 \left( \frac{\rho_0 r}{a_0} \right)$  ( $\rho_0 = 2.4048\dots$ ) intensity profile, i.e., we suppose that all the energy is initially in the  $\text{EH}_{11}$  mode (the fundamental mode of the capillary). In order to take into account the energy losses due to the imperfect coupling of the laser in the capillary, as input energy at the capillary entrance we take the experimental value of the energy transmitted without gas. We then neglect the losses due to the damping of the fundamental mode, which are estimated to be 1.2 % of the input energy. In this condition, the input energy used in the code for He, Ne and Ar is then 27.3, 25.2 and 14.5 mJ, respectively, corresponding to maximum intensities of  $1.7 \times 10^{15}$ ,  $1.6 \times 10^{15}$  and  $7.3 \times 10^{14} \text{ W/cm}^2$ . Since an argon atom is easier to ionize than helium and neon, the experiments with argon gas have been achieved with lower input intensity in order to work in a measurable pressure range. Finally, to compare the numerical results with the experimental data, we compute the far-field spatial, spectral and temporal laser profiles, 2 m behind the capillary, by means of a Hankel transform.

## 5 Results and discussion

### 5.1 Transmitted energy versus gas

Figure 3a–c show the dependence with gas pressure of the transmission in the  $\text{EH}_{11}$  mode of the capillary, for, respectively, He (Fig. 3a), Ne (Fig. 3b) and Ar (Fig. 3c) gases. Experimental points are depicted by full triangles and solid lines while simulations results are represented by means of full squares and dashed lines. We first discuss the experimental data. For He and Ne gases, the transmitted energy at the output capillary without gas is roughly the same, i.e., around 25 mJ. Then, we can directly compare the data obtained with these two gases. Between 0 and 8 mbar He gas pressure, the output energy in the  $\text{EH}_{11}$  mode is divided by a factor of 2, while with Ne gas, a 50 % transmission is obtained for a lower backing pressure,

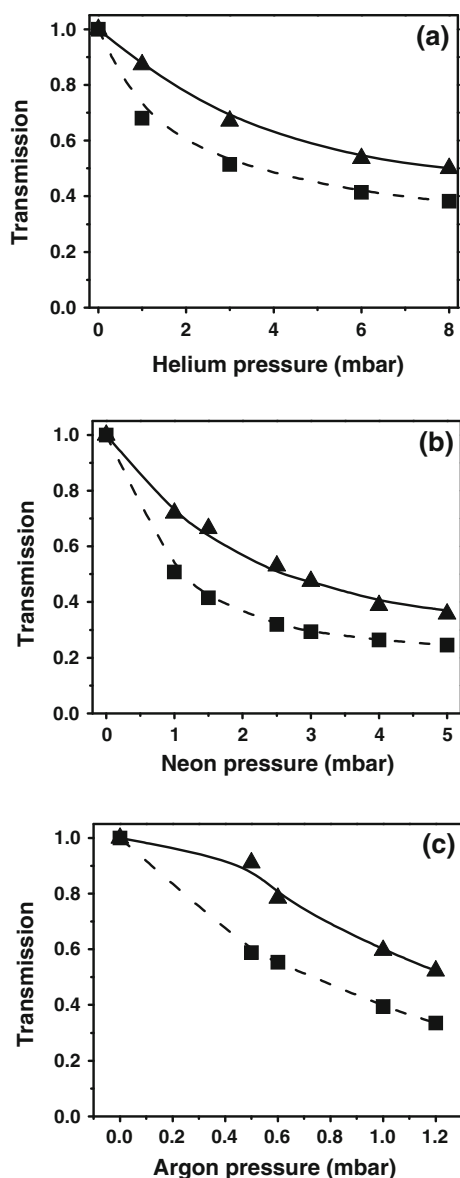


**Fig. 3** Capillary transmission in  $\text{EH}_{11}$  mode as a function of gas pressure for **a** He,  $E_L = 27.3$  mJ,  $\tau_L = 40$  fs, **b** Ne,  $E_L = 25.2$  mJ,  $\tau_L = 40$  fs and **c** Ar,  $E_L = 14.5$  mJ,  $\tau_L = 40$  fs. The hollow capillary radius is  $210 \mu\text{m}$  and the length is  $40$  cm. *Full triangles* experiment. *Full squares* simulations. The *lines* are B-spline fits of the data

between 2.5 and 3 mbar. When increasing neon pressure up to 5 mbar, the output transmission drops to 36 % (corresponding to an output energy of 9 mJ). As expected, at a given gas pressure, the ionization-induced-refraction is stronger in neon than in helium gas, due to the difference on ionization potentials ( $I_P^1 = 24.59$  eV,  $I_P^2 = 54.4$  eV for He and  $I_P^1 = 21.56$  eV,  $I_P^2 = 41.1$  eV for Ne). This behaviour is even more pronounced with argon gas where a 50 % energy transmission is measured for a backing pressure of only 1.2 mbar. Note that in this case, experiments have been performed with a transmitted energy at the capillary output of 14.5 mJ without gas in order to

reduce plasma refraction on one hand, and to observe gas pressure dependence of the capillary transmission for measurable values of pressure on the other.

These results clearly indicate a strong dependence of the gas-filled capillary transmission on the ionization potential of the gas used, suggesting that a compromise between the maximum spectral bandwidth achievable (depending on  $\partial N_e/\partial t$ ) on the one hand, and the energy losses due to ionization (depending on  $\partial N_e/\partial r$ ) on the other must be found. The simulations describe very well the above general trends. However, we note a systematic underestimate of the output energy of about 20 % for He, up to 33 % for Ne and 35 % for Ar. This could be due to an uncertainty on the input energy coupled in capillary modes. As we mentioned in Sect. 4, we take as input energy in the simulations the experimental transmitted energy in  $\text{EH}_{11}$  mode obtained without gas. The latter does not depend a priori on the gas used, except that in the case of Ne and Ar gases, the ionization dynamics is complicated by the production of multiple-charged ions, making the ionization process more sensitive to the input energy. Experimentally, because of the roughness of the inner capillary walls and the spatial quality of the input beam, the energy transmitted by the capillary is not necessarily the energy coupled in the fundamental mode at the capillary entrance. Indeed, the laser pulse while propagating could couple in modes higher than the  $\text{EH}_{11}$  one. These modes are more damped than the fundamental one, even with large diameter capillaries as used here, the damping factor  $\alpha$  scaling as  $1/a_0^3$  ( $\alpha_{11} = 0.0147 \text{ m}^{-1}$ ,  $\alpha_{12} = 0.0774 \text{ m}^{-1}$ ,  $\alpha_{13} = 0.19 \text{ m}^{-1}$  for a  $420 \mu\text{m}$  inner diameter capillary). Moreover, the divergence of the high-modes increases with order and the energy is measured in the far-field, 2 m behind the capillary, with a 15-mm-diameter iris selecting the fundamental mode (Fig. 2). The coupling of the laser pulse in high-modes due to the roughness of the inner walls of the capillary, and to the spatial quality of the input beam, could then cause extra losses in the experiment [37], and hence could lead to an underestimation of the input energy used in the simulations. Finally, as mentioned in Sect. 3, we consider in the simulations a uniformly filled capillary, i.e., we do not take into account tip leaks, which generate longitudinal pressure gradients modifying the transmitted laser energy.

## 5.2 Dependence of spectral broadening with gas

We have reported in Figs. 4, 5, 6 the evolution with pressure of the spectrum measured (a) and calculated (b) 2 m away from the output of the capillary, for each of the three gases used. As expected, for a given gas the spectral bandwidth increases with pressure. A prominent blue-feature, characteristic of OFI-induced spectral broadening,

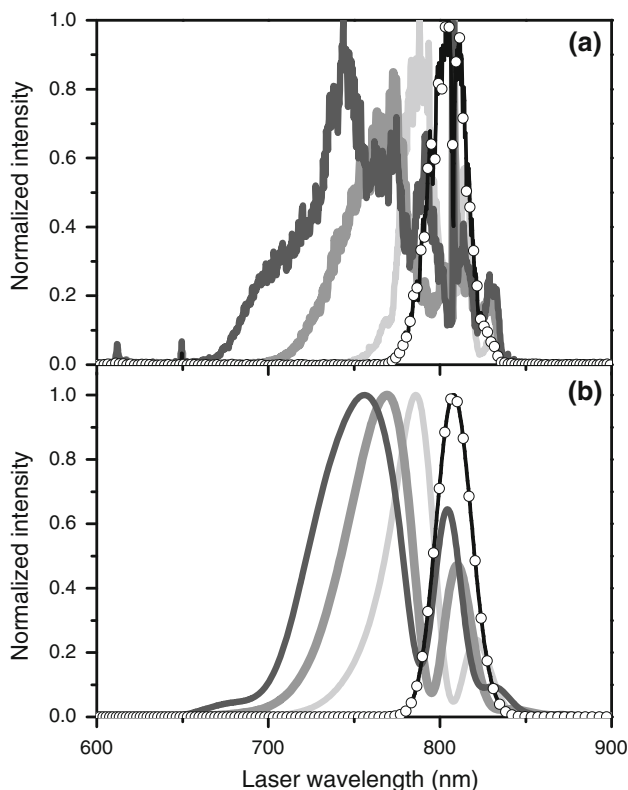


**Fig. 4** Evolution of the output spectrum shape with He pressure for the same conditions as in Fig. 3. **a** Experiment. **b** Simulations. *Open circles + black line* reference without gas. *Light grey solid line*  $p_{\text{He}} = 1.0$  mbar, *Grey solid line*  $p_{\text{He}} = 3.0$  mbar, *Dark grey solid line*  $p_{\text{He}} = 8.0$  mbar

develops and shifts toward shorter wavelengths as the pressure is increased. In the case of He gas (Fig. 4), the spectral broadening by OFI is rather smooth and extends up to 670 nm wavelength when pressure of 8 mbar is used. One can mention that a higher helium pressure does not increase the spectral broadening while it lowers the transmitted energy. For the two other gases used (Figs. 5, 6), broader spectra are observed with lower gas pressures (the wavelengths extending up to 590 nm with 5 mbar Ne and 650 nm with 1.2 mbar Ar), but with strong amplitude modulations, especially in the case of Ar gas (Fig. 6). This can be explained by He ionization potential which is high enough ( $I_p^1 = 24.58$  eV), as compared to those of Ne ( $I_p^1 = 21.56$  eV) and Ar ( $I_p^1 = 15.76$  eV), for producing singly charged ions only. Because of the large ionization potential of the second charge state of He ( $I_p^2 = 54.42$  eV), the time-derivative of the electron density  $\frac{\partial N_e}{\partial t}$ , responsible for the creation of new frequencies, is cancelled once the laser intensity reaches the saturation intensity of the first charge state (evaluated with the barrier-suppression-ionization (BSI) model [38], we obtain  $I_s = 1.5 \times 10^{15}$  W/cm<sup>2</sup> for He atom), making the ionization dynamics much simpler than with Ne and Ar. In the two latter cases,

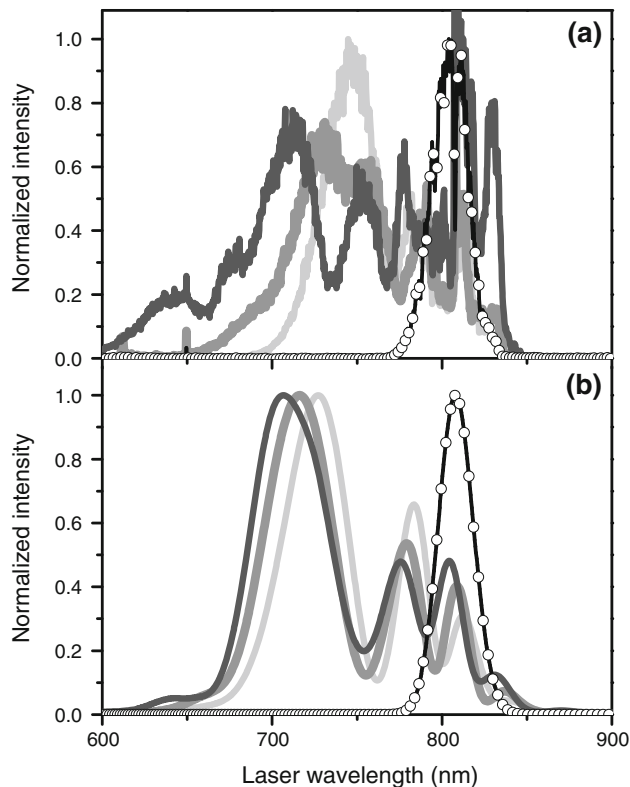


**Fig. 5** Evolution of the output spectrum shape with Ne pressure for the same conditions as in Fig. 3. **a** Experiment. **b** Simulations. *Open circles + black line* reference without gas. *Light grey solid line*  $p_{\text{Ne}} = 1.5$  mbar, *Grey solid line*  $p_{\text{Ne}} = 2.5$  mbar, *Dark grey solid line*  $p_{\text{Ne}} = 5.0$  mbar

multiply charged ions are produced up to the maximum laser intensity, and thus the electron density could always increase with time on the leading front of the pulse. Moreover, the value of the time-derivative  $\frac{\partial N_e}{\partial t}$  changes between two consecutive ionization charge states, the slope depending on the ionization potential, the pulse rise time, and the peak intensity: the shorter the plasma density rise time, the more the wavelength is blue-shifted. Experimentally, we observed that a reduction of the input energy leads to a decrease of the spectral bandwidth and the amplitude modulations.

When fully taking into account spatio-temporal couplings, a very good agreement between the computed and the experimental spectra is obtained for the three different gases used. The 3D model could reproduce the number and the position of peaks in the blue-wing of the spectra in the full range of pressure (Figs. 4b, 5b, 6b), even though the energy transmitted by the capillary is underestimated in the calculations. It has also to be noted that the spectral broadening given by the 3D code is less than that predicted by 1D Eq. 1. This is actually due to three-dimension effects. Indeed, the 3D simulations show that the ionizing laser beam, when propagating inside the gas-filled

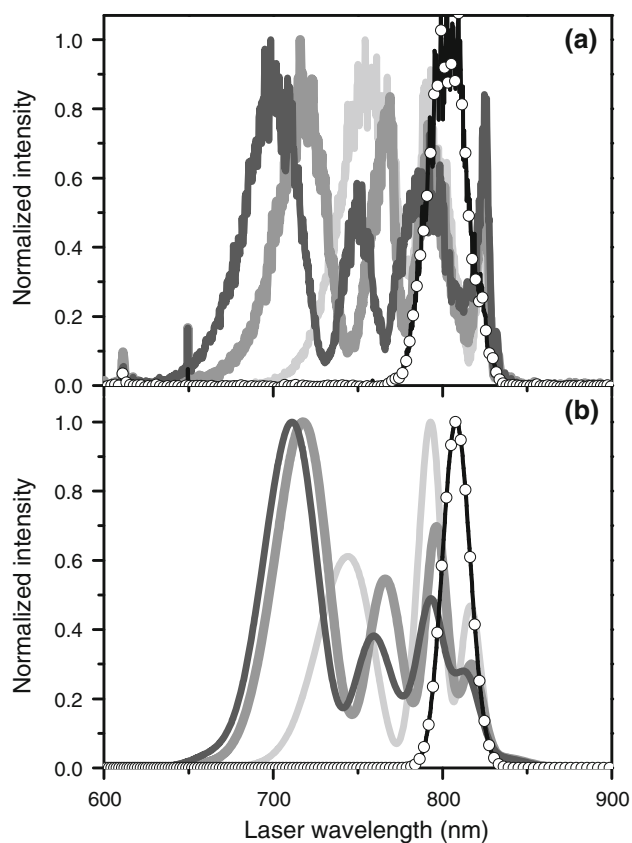


**Fig. 6** Evolution of the output spectrum shape with Ar pressure for the same conditions as in Fig. 3. **a** Experiment. **b** Simulations. *Open circles + black line*: reference without gas. *Light grey solid line*  $p_{\text{Ar}} = 0.5$  mbar, *Grey solid line*  $p_{\text{Ar}} = 1.0$  mbar, *Dark grey solid line*  $p_{\text{Ar}} = 1.2$  mbar

capillary, is alternatively focused and refracted, and generates strongly inhomogeneous plasma, in the propagation direction (as discussed in Sect. 5.3). Ionization, as a highly non-linear process, couples the beam into high-order modes producing strong modulations of the intensity with an alternation of peaks and zeros. The number of coupled modes increases with pressure, and also with the degree of ionization of the plasma. On the other hand, the ionization, which occurs on the leading front of the pulse, modifies dramatically the trailing edge. The latter divides into several pulses, which propagate with different group velocities. The peak laser intensity then decreases with the propagation distance inside the capillary. All these effects are strongly dependent on the gas used: at given intensity, the lower the ionization potential, the earlier the first electrons are released and the higher the ionization state. Then, depending on the gas and/or the input pulse intensity, the energy transmission of the capillary and the spectral broadening achieved are coupled, but for quite different pressures. For example, a spectral broadening with a blue wing extending up to 670 nm requires gas pressures of

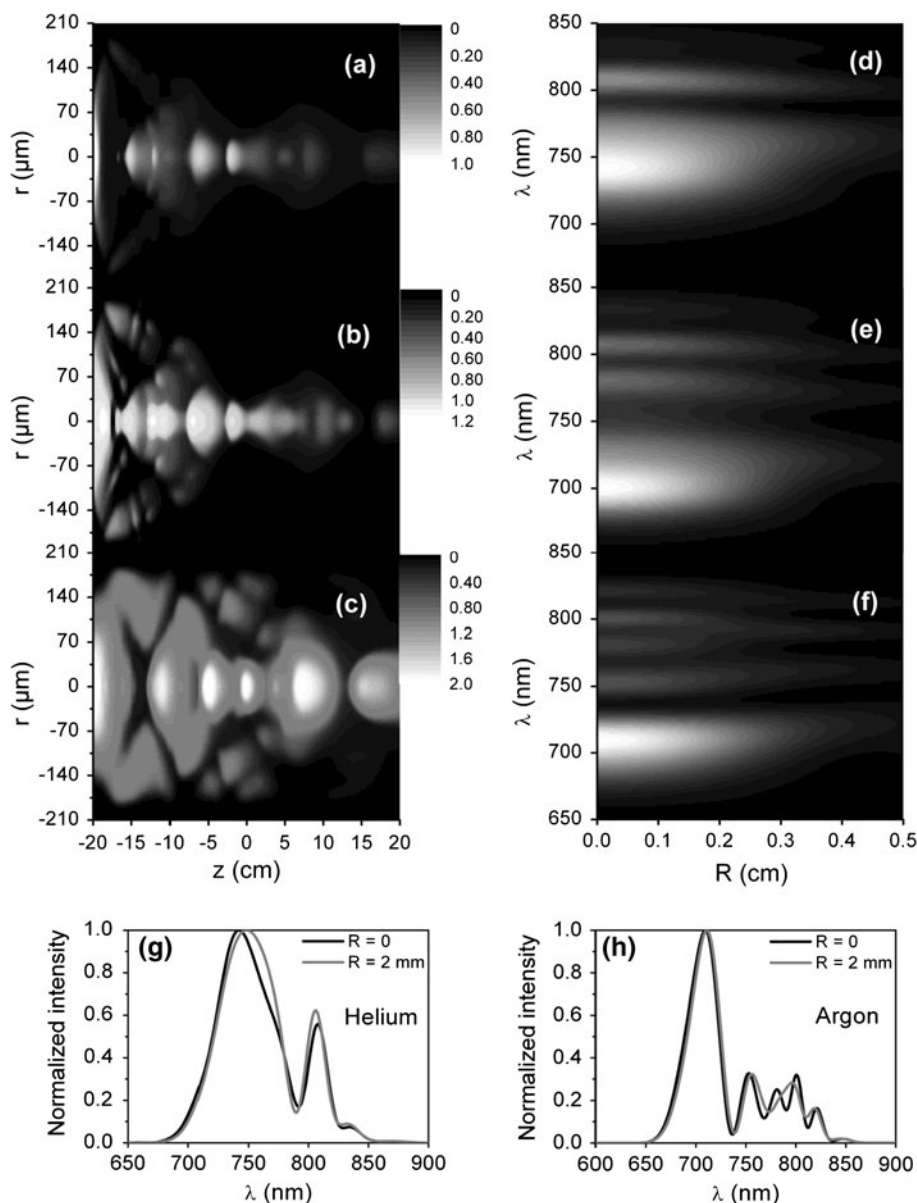
8 mbar He, 2.5 mbar Ne and 1.2 mbar Ar, for roughly the same value of energy transmission, i.e., 50 %.

### 5.3 Plasma homogeneity in the capillary and spatial uniformity of the spectral broadening

Since the high energy post-compression technique has been developed to provide driving laser sources for HHG, the spatial uniformity of the output beam characteristics is a crucial point. Therefore, by using the 3D code, we have investigated the plasma homogeneity as well as the spatially resolved spectrum of the output pulse in the far field. Spatially resolved ionization charge state and far-field spectra are given in Fig. 7 for the three gases. In each case, the spectral intensity is normalized to the maximum. The maps in Fig. 7a, d have been calculated for 8 mbar helium gas pressure, whereas data in Fig. 7b, e, and c, f have been obtained for 5 mbar neon gas pressure, and 1.2 mbar argon gas pressure, respectively. Other conditions are the same as in Fig. 3. Despite some strong inhomogeneities in the plasma profile, resulting from the beating between high excited modes of the capillary, the most striking feature is that, whatever the gas used, far-field spectra have a good radial homogeneity as shown on the on- and off-axis spectral shapes given in Fig. 7g, h for He and Ar gases, respectively. With He gas, the maximum degree of ionization reaches 1 only on a small fraction of the capillary length (Fig. 7a), leading to a spectrum with two distinct components: a red unshifted component (around 808 nm wavelength) and a blue broadband one, around 750 nm wavelength. For Ne gas, the size of the plasma is bigger than with He gas, in both radial and longitudinal directions (Fig. 7b), with a maximum charge state of 1.2. In the (initial) spectral range of the ionizing pulse, a third peak appears near 780 nm wavelength (Fig. 7e) and the blue feature peaks around 700 nm wavelength. The unshifted spectral component gets weaker, indicating that a larger portion of the pulse (as compared to the case of He) is involved in the ionization process. This interpretation is supported by the observation of the decrease of energy transmission between He and Ne gases, due to the refraction of the beam while ionizing the gas (Fig. 3a, b). In the case of Ar gas, the effect is even more pronounced than in the two other cases. The maximum degree of ionization reaches 2, and is achieved very close to the output of the capillary (Fig. 7c), leading to a redistribution of laser energy between five peaks, in the 700–825 nm wavelength range (Fig. 7f). In terms of mode coupling, the excitation of high modes occurs on the entire length of the capillary when filled with Ar gas, whereas this occurs roughly on the first half of the length when using He gas.



**Fig. 7** Spatially resolved ionization charge state and far-field spectrum of the output pulse computed for 8 mbar He (**a, d**), 5 mbar Ne (**b, e**) and 1.2 mbar Ar (**c, f**). **g, h** Output far-field spectrum on-axis (*black line*) and 2 mm off-axis (*grey line*), for, respectively, He and Ar gases. See the text for details about the laser energy



#### 5.4 Post-compressed pulse duration as a function of gas

The optimal duration of post-compressed pulses as a function of gas pressure is shown in Fig. 8 for He (Fig. 8a), Ne (Fig. 8b) and Ar (Fig. 8c). They are measured at full-width at half-maximum of the temporal profiles. The curves depicted by a solid line and full triangles correspond to experimental measurements performed with a single-shot autocorrelator. The dashed lines and full squares give the simulation results. The latter are inferred from the spectra computed in the far-field, 2 m behind the capillary, on the laser axis. To simulate the post-compression process by the chirped-mirrors, we proceed as follows. We first subtract the linear component and add a quadratic term to the spectral phase in order to cancel the second-order

component resulting from the self-phase-modulation of the ionizing pulse. Finally, we calculate the temporal profile as the Fourier transform of the electric field (residual phase and amplitude) in the spectral domain.

As a general trend, the post-compressed pulse duration first decreases strongly with gas pressure in the range 0–3 mbar for He, 0–1 mbar for Ne and 0–0.5 mbar for Ar, where the pulse duration is divided by a factor of 2. When increasing the pressure, the latter decreases asymptotically to its minimum value around 10–11 fs. For He gas, the shortest post-compressed pulse duration experimentally achieved is 11.4 fs (FWHM). It is obtained with 8 mbar pressure, leading to a post-compression factor (defined as the ratio of the final post-compressed pulse duration to the initial 40 fs duration of the input pulse) of 3.5. The values

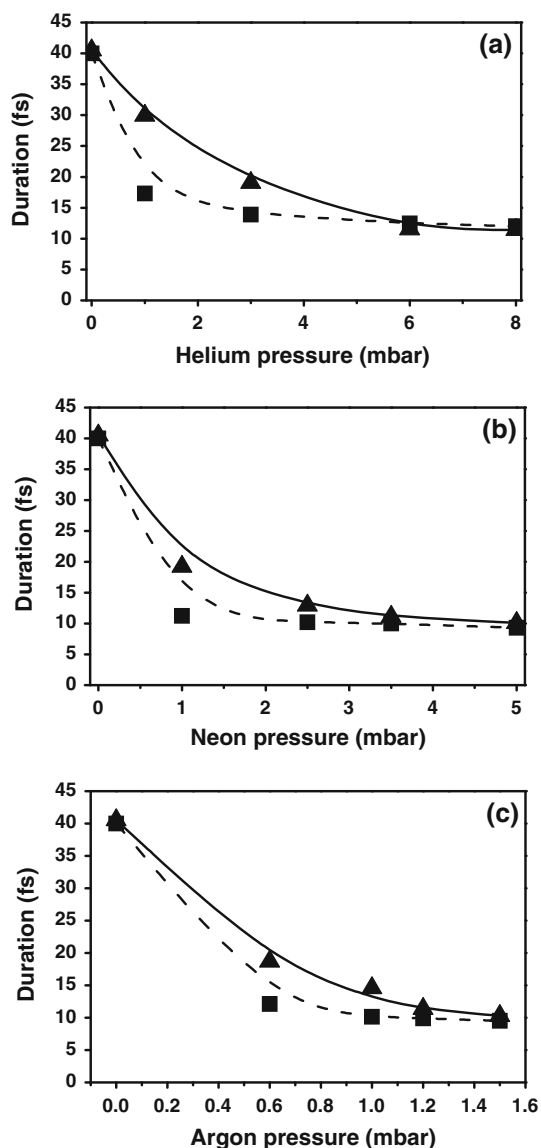


**Fig. 8** Optimal duration of post-compressed pulses as a function of gas pressure obtained with **a** He, **b** Ne and **c** Ar gases. Other conditions are the same as in Fig. 3. *Full triangles* experiment. *Full squares* simulations. The *lines* are B-spline fits of the data

deduced from the simulations are in fairly good agreement with experimental data, except for the point at 1 mbar. In this case, the discrepancy is likely due to the experimental uncertainty on pressure gradients, due to tip losses, together with the rapid variation of the post-compressed pulse duration at low pressures. The shortest duration given by the simulations is 12 fs and is achieved with 8 mbar pressure. If we now turn our attention to the results obtained with Ne gas, we see that, experimentally, the minimum post-compressed pulse duration is 10.1 fs and is obtained for 5 mbar pressure. This is shorter than that achieved with He gas but the transmission is lower ( $\sim 36\%$ ). A pulse duration of 11.4 fs with a transmitted

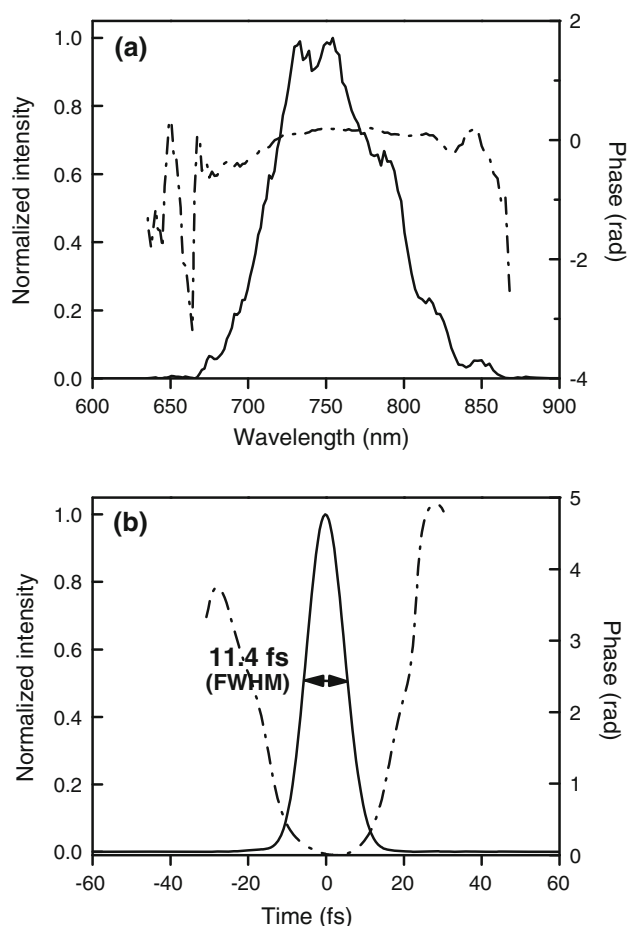


**Fig. 9** SHG-FROG measurement of the shortest post-compressed pulse obtained with 8.0 mbar He pressure, 70 mJ laser energy and 40 fs initial pulse duration. **a** Retrieved (*solid curve*) spectra of the post-compressed pulse with the residual spectral phase (*dashed-dotted curve*). **b** Retrieved intensity profile (*solid curve*) and temporal phase (*dashed-dotted curve*) of the post-compressed pulses

energy close to 50 % (the minimum post-compressed pulse duration and the maximum transmission, reached with 8 mbar He pressure) are achieved around 3 mbar Ne pressure. The computed durations are again in good agreement with experimental data. Finally, we have carried out a systematic study with Ar gas and measured pulse duration as short as 10.3 fs for 1.5 mbar pressure. Post-compressed pulse duration of 11.4 fs, with 50 % energy transmission, is then achieved for 1.2 mbar pressure. Therefore, even with different laser intensities, the performances of the OFI post-compression technique are very similar if the gas and the operating pressure are judiciously chosen. One can mention that in all three gases, the optimized dispersion compensation to obtain the shortest pulse duration in the experiment is roughly the same value, which is around  $-150 \text{ fs}^2$ . In the simulations, the optimum value is about  $-90 \text{ fs}^2$  whatever the gas used.

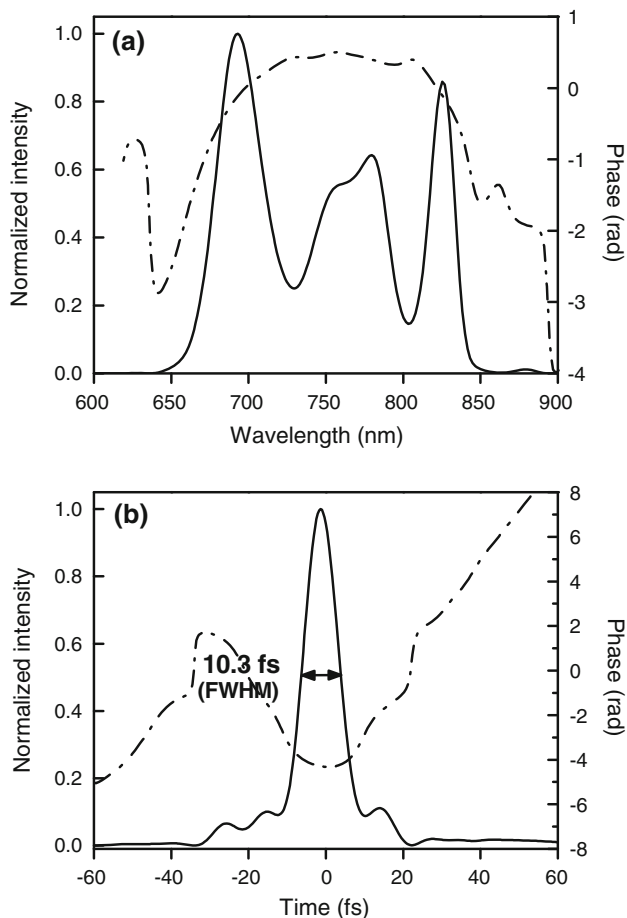


**Fig. 10** SHG-FROG measurement of the shortest post-compressed pulse obtained with 1.5 mbar Ar pressure, 37 mJ laser energy and 40-fs initial pulse duration. **a** Retrieved (solid curve) spectra of the post-compressed pulse with the residual spectral phase (dashed-dotted curve). **b** Retrieved intensity profile (solid curve) and temporal phase (dashed-dotted curve) of the post-compressed pulses

In order to characterize the quality of the post-compressed pulses in terms of residual spectral phase and shape, we performed single-shot measurements with a SHG-FROG in the two extreme cases that are helium at 8 mbar (Fig. 9) and argon at 1.5 mbar (Fig. 10). Figures 9a and 10a show the retrieved spectra with the residual spectral phase and Figs 9b and 10b give the intensity profile of the post-compressed pulse. In both cases, we observe some residual spectral phase, which does not affect the optimal pulse duration if one compares to the Fourier transform of the experimental spectrum. However, we can observe a lower pedestal on the reconstructed temporal pulse profile in He than in Ar gas. In this latter case, the temporal contrast is mainly limited by the deep amplitude modulations in the spectrum (as confirmed by the Fourier transform of the spectrum). Nevertheless, the timescale during which the pedestal level is significant ( $\sim 10^{-1}$ – $10^{-2}$  of the peak intensity) is short ( $\sim 50$ – $100$  fs), and the

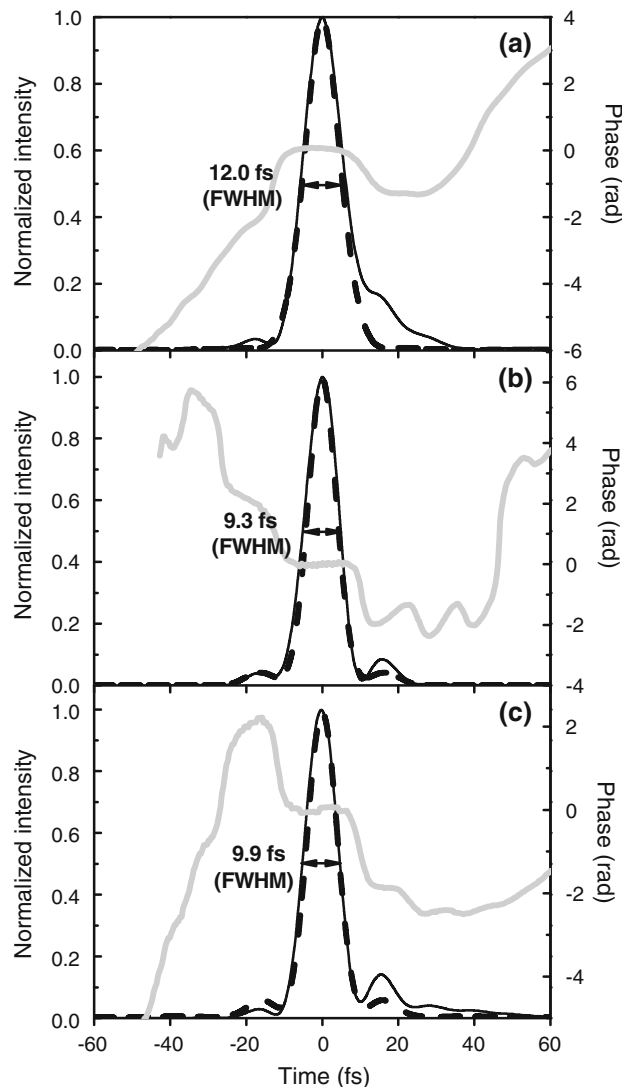


**Fig. 11** Time profiles of post-compressed pulse calculated on the laser axis in the far-field and corresponding to optimal durations in 8 mbar He (**a**), in 3.5 mbar Ne (**b**) and 1.2 mbar Ar (**c**). Solid line Temporal profile after compensation of the quadratic component of the spectral phase. Light grey solid line residual temporal phase, dashed line Fourier-transform limit of the computed spectral amplitude

energy in the main pulse is 79 % in the case of Ar gas. This trend is confirmed by numerical results where ripples are observed on both the leading and the trailing edges of the temporal profiles presented in Fig. 11a–c, for 8 mbar He, 3.5 mbar Ne and 1.2 mbar Ar pressures, respectively. The solid lines depict the temporal shapes obtained after cancellation of the second-order component of the spectral phase whereas the dashed lines correspond to the profiles calculated with a constant spectral phase (Fourier transform). Both temporal profiles are very close to each other in the central part of the pulse whatever the gas used. The pedestal comes from uncompensated spectral phase

components and from spectral amplitude modulations. Finally, the energy contained in the main peak is quite similar for He and Ne gases, with, respectively, 89 and 92 % of the total energy in the pulse, and is slightly less for Ar gas with 80 % of the energy. By taking into account the 13.7 mJ energy transmitted by the capillary at 8 mbar helium gas pressure and the FROG temporal pulse profile, the peak power of the post-compressed pulse reaches 1.12 TW.

## 6 Conclusion

In summary, we have reported a thorough experimental and numerical study on a post-compression technique using optical-field-ionization of noble gases as a mechanism for broadening the spectrum of the initial pulse. The influence of the gas used on the transmitted energies and spectral shapes, and on the subsequent post-compressed pulse durations has been investigated. Even in the multi-ionization regime, we have demonstrated, both experimentally and numerically, that OFI post-compression technique works with a compression factor around 3.5–4 while preserving the laser peak power. Despite some strong modulations of the spectral amplitude, the spectral phase resulting from optical-field-ionization induced SPM in a low pressure gas-filled hollow capillary remains mainly quadratic even in the multi-ionization regime. Therefore, shorter pulse duration was achieved with Ne and Ar gases, but to the detriment of the energy transmission in the EH<sub>11</sub> capillary mode. Compared to He gas, it was shown that due to a smaller ionization potential, Ar gas (and to a lesser extent Ne gas) becomes highly ionized, multi-ionization enhancing the spectral broadening but giving rise to larger energy losses due to OFI-induced refraction. However, for a given spectral broadening or compression factor, the capillary transmission is the same whatever the gas used, except that the filling pressure must be adjusted. The slight difference when multi-ionization dynamics takes place is the pedestal level and the energy contained in the main peak. Nevertheless, the robustness of the post-compression technique demonstrated here, with regard to multi-ionization, suggests that it could be extrapolated to a large range of interaction intensities consistent with high-repetition rate femtosecond laser systems providing pulse energy larger than 10 mJ. Since high intensity can propagate in hollow dielectric capillaries without wall glass breakdown [39], the most attractive interest of this technique is the up-scaling in energy to a few hundred millijoules level by using the double ionization of helium with interaction intensities of few  $10^{16}$  W/cm<sup>2</sup>. This configuration should offer the opportunity to provide multi-10 TW with few

optical cycle pulse durations from conventional CPA Ti:Sapphire laser systems.

**Acknowledgments** The authors thank C. Medina, R. Bouillaud, and L. Merzeau for their technical assistance. This work is supported by the Conseil Régional d'Aquitaine (COLA2 2.1.3 09010502), the European Union (EU) (LaserLabII ALADIN) and the Agence Nationale de la Recherche (ANR-09- BLAN-0031-02).

## References

1. F. Krausz, M. Ivanov, *Rev. Mod. Phys.* **81**, 163 (2009)
2. M. Nisoli, S. Sansone, *Prog. Quantum Electron.* **33**, 17 (2009)
3. P. Corkum, N. Burnett, M. Ivanov, *Opt. Lett.* **19**, 1870 (1994)
4. I. Christov, M. Murnane, H. Kapteyn, *Phys. Rev. Lett.* **78**, 1251 (1997)
5. G. Tsakiris, K. Eidmann, J. Meyer-ter-Vehn, F. Krausz, *New J. Phys.* **8**, 19 (2006)
6. V.V. Strelkov, E. Mével, E. Constant, *New J. Phys.* **10**, 083040 (2008)
7. E. Goulielmakis, V.S. Yakovlev, A.L. Cavalieri, M. Uiberacker, V. Pervak, A. Apolonski, R. Kienberger, U. Kleineberg, F. Krausz, *Science* **320**, 1614 (2008)
8. F. Ferrari, F. Calegari, M. Lucchini, C. Vozzi, S. Stagira, G. Sansone, M. Nisoli, *Nat. Photonics* **4**, 875 (2010)
9. P. Heissler, R. Hörlein, J.M. Mikhailova, L. Waldecker, P. Tzallas, A. Buck, K. Schmid, C.M.S. Sears, F. Krausz, L. Veisz, M. Zepf, G.D. Tsakiris, *Phys. Rev. Lett.* **108**, 235003 (2012)
10. M. Hentschel, R. Kienberger, Ch. Spielmann, G.A. Reider, N. Milosevic, T. Brabec, P. Corkum, U. Heinzmann, M. Drescher, F. Krausz, *Nature* **414**, 509 (2001)
11. M. Drescher, M. Hentschel, R. Kienberger, M. Uiberacker, V. Yakovlev, A. Scrinzi, Th Westerwalbesloh, U. Kleineberg, U. Heinzmann, F. Krausz, *Nature* **419**, 803 (2002)
12. R. Kienberger, E. Goulielmakis, M. Uiberacker, A. Baltuska, V. Yakovlev, F. Bammer, A. Scrinzi, Th Westerwalbesloh, U. Kleineberg, U. Heinzmann, M. Drescher, F. Krausz, *Nature* **427**, 817 (2004)
13. E. Goulielmakis, V.S. Yakovlev, A.L. Cavalieri, M. Uiberacker, V. Pervak, A. Apolonski, R. Kienberger, U. Kleineberg, F. Krausz, *Science* **317**, 769 (2007)
14. C. Hauri, W. Kornelis, F. Heinrich, A. Couairon, A. Mysyrowicz, J. Biegert, U. Keller, *Appl. Phys. B* **79**, 673 (2004)
15. M. Nisoli, S. De Silvestri, O. Svelto, *Appl. Phys. Lett.* **68**, 2793 (1996)
16. M. Nisoli, S. Stagira, S. De Silvestri, O. Svelto, S. Sartania, Z. Cheng, M. Lenzner, Ch. Spielmann, F. Krausz, *Appl. Phys. B* **65**, 189 (1997)
17. S. Bohman, A. Suda, T. Kanai, S. Yamaguchi, K. Midorikawa, *Opt. Lett.* **35**, 1887 (2010)
18. X. Chen, A. Malvache, A. Ricci, A. Jullien, R. Lopez-Martens, *Laser Phys.* **21**, 198 (2011)
19. G. Tempea, T. Brabec, *Opt. Lett.* **23**, 762 (1998)
20. A. Couairon, S. Tzortzakis, L. Bergé, M. Franco, B. Prade, A. Mysyrowicz, *J. Opt. Soc. Am. B* **19**, 1117 (2002)
21. N. Ishii, L. Turi, V.S. Yakovlev, T. Fuji, F. Krausz, A. Baltuska, R. Butkus, G. Veitas, V. Smilgevicius, R. Danielius, A. Piskarskas, *Opt. Lett.* **30**, 567 (2005)
22. F. Tavella, A. Marcinkevicius, F. Krausz, *Opt. Express* **14**, 12822 (2006)
23. D. Herrmann, L. Veisz, R. Tautz, F. Tavella, K. Schmid, V. Pervak, F. Krausz, *Opt. Lett.* **34**, 2459 (2009)

24. C. Fourcade Dutin, A. Dubrouil, S. Petit, E. Mével, E. Constant, D. Descamps, *Opt. Lett.* **35**, 253 (2010)
25. T. Auguste, O. Gobert, C. Fourcade Dutin, A. Dubrouil, S. Petit, E. Mével, E. Constant, D. Descamps, *J. Opt. Soc. Am. B.* **29**, 1277 (2012)
26. E. Yablonovitch, *Phys. Rev. Lett.* **60**, 795 (1988)
27. A.M. Perelomov, V.S. Popov, M.V. Terent'ev, *Sov. Phys. JETP* **23**, 924 (1966)
28. A.M. Perelomov, V.S. Popov, M.V. Terent'ev, *Sov. Phys. JETP* **24**, 207 (1967)
29. A. Perelomov, V. Popov, *Sov. Phys. JETP* **25**, 336 (1967)
30. M.V. Ammosov, N.B. Delone, V.P. Krainov, *Sov. Phys. JETP* **64**, 1191 (1986)
31. T. Auguste, P. Monot, L.-A. Lompré, G. Mainfray, C. Manus, *Opt. Commun.* **89**, 145 (1992)
32. E.A. Marcatili, R.A. Schmelzter, *Bell Syst. Tech. J.* **43**, 1783 (1964)
33. R. Trebino, K. Delong, D. Fittinghoff, J. Sweetser, M. Krumbiegel, B. Richman, D. Kane, *Rev. Sci. Instrum.* **68**, 3277 (1997)
34. L. Bergé, S. Skupin, R. Nuter, J. Kasparian, J.-P. Wolf, *Rep. Prog. Phys.* **70**, 1633 (2007)
35. M. Nurhuda, A. Suda, K. Midorikawa, M. Hatayama, K. Nagasaka, *J. Opt. Soc. Am. B* **20**, 2002 (2003)
36. W.H. Press, S.A. Teukolsky, W.T. Vetterling, B.P. Flannery, *Numerical Recipes in Fortran* (Cambridge University, Cambridge, 1992), pp. 701–740
37. O.B. Danilov, M.I. Zintchenko, YuA Rubinov, E.N. Sosnov, *J. Opt. Soc. Am. B* **7**, 1785 (1990)
38. S. Augst, D. Strickland, D.D. Meyerhofer, S.L. Chin, J.H. Eberly, *Phys. Rev. Lett.* **63**, 2212 (1989)
39. C. Courtois, B. Cros, G. Malka, G. Matthieussent, J.R. Marquès, N. Blanchot, J.L. Miquel, *J. Opt. Soc. Am. B* **17**, 864 (2000)